A MORPHOLOGICAL APPROACH OF FALSE STAR REMOVAL AND CAMERA MOTION ESTIMATION FOR STAR SENSORS

Erdem Onur OZYURT[1)], Alim Rustem ASLAN[1)],
[1)] *Space Systems Design and Test Laboratory, Istanbul Technical University, Istanbul, Turkey*
ozyurter@itu.edu.tr, aslanr@itu.edu.tr

A demand of high accuracy settles attitude determination and control systems, which CubeSats rely on for success of a mission, into a vital role. A star sensor is a prominent choice in attitude determination because of its capability of high accuracy and its usability at any point in space independently from any celestial body. The process of star identification is a key phase within the implementation of attitude determination, in which an observed body vector is transformed into a vector defined in the inertial frame. However, the sources of noise injected on the observed vector challenges the accuracy of star identification outputs due to fallacies in the phase of star detection and centroiding prior to star identification. Accuracy in the process of star detection and centroiding may vary, besides the sources of noise, with the properties of star sensors including field-of-view, resolution and saturation sensitivity. The improvements cost, quality, success and lifetime of a CubeSat space mission may be ensured through noise removal implemented in the phase of star detection, centroiding or star identification, which would lead to higher accuracy and less complexity, thus helping decrease storage and memory space. Furthermore, as to the standards of the European Space Agency, a star sensor is required to resume operating in the presence of non-star objects in the field-of-view or solar flare which induces high energy protons to interact with the imaging field, which are regarded as sources of noise. The sources of noise involve false stars due to reflecting objects and solar flare, shifted stars due to thermal deformation or optical flaws and missing stars due to blockage of field-of-view and dead pixels. These phenomena pose a threat against high accuracy; thus, they are required to be removed where possible.

This study aims removal of false stars using a morphological approach, which is followed by estimation of camera motion between two image frames. The proposed method is based on isomorphism through matching the star pairs in at least two consecutive image frames. The detection of false stars also allows estimation of translational and rotational motion of the star sensor camera. The implementation is carried out by setting feature vectors involving the average luminous magnitude of star pair, the angular separation of star pair and the slope of star pair for each pair of stars in each frame and setting a list of disparities containing Euclidean distances between each pair of feature vectors selected from two different consecutive frames. The disparity vectors are used to determine the star objects and to label non-star objects, as well as to retrieve the motion parameters, including translation and rotation. The features of the star sensor camera CubeStar used in the project SharjahSat-1 is simulated in the experimental setup of this study. The effectiveness and accuracy of the method is revealed in the empirical results, and the additional motion estimation parameters are planned to be used in future studies of star identification.

Key Words: Attitude Determination, Star Sensor, False Star Removal, Camera Motion Estimation

1. Overview

This study focuses on removal of false stars using a morphological approach, which is followed by estimation of camera motion between two image frames. The proposed method is based on isomorphism through matching the star pairs in at least two consecutive image frames. The detection of false stars also allows estimation of translational and rotational motion of the star sensor camera. Subsequent to detection of stars and centroiding, a set of feature vectors is obtained for each pair of stars in each frame. A feature vector comprises three elements including the average luminous magnitude of star pair, the angular separation of star pair and the slope of star pair. Thereafter, a list of disparities is set, which contains Euclidean distances between each pair of feature vectors, each of which is selected from two different consecutive frames. A disparity in the list also comprises vectors of three elements. The first two elements in the disparity vector are used to determine the star objects and to label non-star objects, while the third element is also used to retrieve the motion parameters, including translation and rotation. This is achieved by means of tolerances corresponding to luminous magnitude and angular separation to take the presence of noise of shifted stars into account. A pair is assumed to be of star objects in case the pair satisfies criteria enforced by tolerances. Having detected star objects in the frames, it is verified whether the third elements of disparity vectors corresponding to the pairs of star objects lie within the given tolerance. An object that is not involved in any of the pairs satisfying the criterion is labeled as a non-star object. Finally, an estimation of rotational camera motion is derived since it holds information of slope change. Also, the translational motion is retrieved by calculating the difference between the labeled star objects after reversing the rotational motion in the latter image frame. The project SharjahSat-1[1)] uses the star sensor camera CubeStar[2)], which is simulated in the experimental setup of this study. The effectiveness and accuracy of the method is revealed in the empirical results, and the additional motion estimation parameters are planned to be used in future studies of star identification.

2. Related Works

Star identification includes image preprocessing, feature extraction and matching. Of them, image preprocessing involves two steps including noise removal and centroiding. Mostly, the center of gravity method yields the fastest results for centroiding despite a reduction in accuracy due to sensitiveness to noise[3)]. Noise is, mostly, removed by linear filtering, median filtering, morphological filtering or etc[4)]. The types of input noise, to which a star sensor is subject, include positional noise, missing and false stars as well as magnitude noise[5)]. Positional noise may emerge due to thermal deformation, optical flaws or calibration errors, while magnitude noise is incurred by the sensitivity of the sensor.

Interfering stars include false stars and missing stars respectively caused by reflecting objects in the field-of-view (FOV) and solar flare and blockages in the FOV and dead pixels. Recent studies analyzed the performance of the proposed star identification methods for their robustness against false star noise[6-8], or simulators were developed to make noise injection including false stars[9]. Lastly, a study proposed a false star filtering algorithm to be used as a preprocessing algorithm for existing star identification algorithms, which utilizes the difference between motion of objects in the FOV by implementing angular distance tracking and star voting on multiple consecutive frames[10].

3. Preliminaries

In this work, the stellar images are simulated using the features of CubeStar which is a miniature star tracker specifically intended for, but not limited to low-power, performance-critical CubeSat applications[2]. The relevant features used in the simulation are given in Table 1. Note that the magnitude limit is arbitrarily specified for a better representation and illustration of results of the study while the onboard star catalog of CubeStar, in fact, comprises a reduced list of the Hipparcos catalog containing 410 stars brighter than 3.8 Vmag.

Table 1. The optical features of CubeStar simulated in the study.

FOV	42° × 42°
Resolution	937px × 937px
Magnitude Limit	> 12.6 Vmag
Mass	55 grams

The Hipparcos Star Catalog[11], which contains high-quality scientific data of 118,218 stars, is used in the implementation of a simulator in this work. The catalog provides the user with several characteristics of each star defined in the International Celestial Reference System (ICRS) with an epoch of J1991.25. In this work, the information of position and magnitude is used. The entries used in the simulation are shown in Table 2. The positional information contains right ascension $\alpha \in (0^o, 360^o)$ and declination $\delta \in (-90^o, 90^o)$, both in degrees. Plus, magnitude information is given in Johnson UBV Photometric System. The feature vectors used for matching and labeling stars in this study contain the positional and magnitude elements as given in the catalog.

Table 2. Entries from the Hipparcos catalog.

Label	Symbol	Description	Field	Unit
HIP	-	Identifier	H1	-
V	V_{mag}	Magnitude	H5	mag
RA	α	Right ascension	H8	deg
Dec	δ	Declination	H9	deg

4. Methodology

The denoising process to be implemented is simply a false star removal. A subgraph isomorphism approach is employed on two consecutive images. This approach requires two sets of feature vectors separately obtained from two consecutive images. Using two sets of feature vectors, a list of disparity vectors is derived. The disparity vectors are obtained by calculating the norm of the difference between each pair of feature vectors in two separate sets obtained from the consecutive images. The disparity vectors satisfying the given criteria are labeled as star objects, namely true stars, while the ones failing the criteria are labeled as non-star objects, namely false stars.

4.1. Feature Extraction

Prior to implementation of subgraph isomorphism, a set of feature vectors are extracted for each consecutive image. The feature vectors contain the slope of the line segments connecting each pair of stars with given centroid and magnitude separately for some consecutive test images as illustrated in Fig. 1.

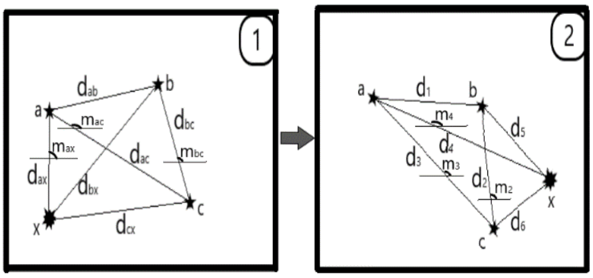

Fig. 1. Pairs of stars in two consecutive test images.

Note that the objects labeled as a, b and c are star objects, whereas the object labeled as x is assumed to be a non-star object in Fig. 1. The line segments d_{ab}, d_{ac}, d_{bc}, d_{ax}, d_{bx} and d_{cx} represent the angular separations between the corresponding objects, and m_{ab}, m_{ac}, m_{bc}, m_{ax}, m_{bx} and m_{cx} denote the slope of the corresponding line segments with respect to a line assumed to be horizontally aligned with respect to the frame plane. Thus, a feature vector is defined such that

$$\vec{v} = \begin{pmatrix} A \\ d \\ m \end{pmatrix}$$

where A, d and m denote the average magnitude, angular separation and slope respectively. In each image frame with N detected objects, the number of pairs of stars is calculated by

$$L = C(N, 2) = \frac{N!}{(N-2)! \cdot 2!}$$

which also yields the number of feature vectors set for each image frame.

4.2. Generation of Disparity List

Two sets of feature vectors are obtained from two consecutive image frames separately. Selecting two arbitrary vectors $\vec{v_i}^t$ and $\vec{v_j}^{t+1}$ from the feature vector sets of the image at time t and at time $t+1$, a new vector set is generated by calculating the norm of the difference between each pair of vectors such that

$$||\vec{v_i}^t - \vec{v_j}^{t+1}|| = \begin{pmatrix} \varDelta A_{ij} \\ \varDelta d_{ij} \\ \varDelta m_{ij} \end{pmatrix}$$

where $\varDelta A_{ij}$, $\varDelta d_{ij}$ and $\varDelta m_{ij}$ respectively correspond to difference of magnitudes, difference of angular separations and rotation. Considering that there are L_1 and L_2 feature vectors in the image frames, the number of vectors in the disparity list is calculated by

$$D = L_1 \times L_2$$

where D is the number of vectors in the disparity list.

4.3. Star Labeling and Motion Estimation

Having generated the disparity list, the elements in the list satisfying the criteria

$$\begin{matrix} \Delta A_{ij} < \epsilon_A \\ \Delta d_{ij} < \epsilon_d \end{matrix} \xrightarrow{yields} \overrightarrow{o_k}\ star\ objects$$

are considered to point to star objects, where ϵ_A and ϵ_d are tolerances corresponding to the relevant value. Also, another criterion is checked to verify the labeling, whether the labeled stars are accumulated satisfying that

$$\|\Delta m_{ij} - s\| < \epsilon_m$$

where s is the difference of slopes and ϵ_m is the slope tolerance. In this regard, the value s yields the amount of rotational motion if it is converted to an angular value θ by means of

$$\theta = \tan^{-1} s$$

where tan^{-1} is the inverse tangent function. Lastly, by reverse rotating the second image and calculating the number of pixels between the identically labeled star objects, the amount of translational motion ρ is also yielded. Thus, the motion estimation is represented by the vector

$$\tilde{\vartheta} = \begin{pmatrix} \tilde{\rho} \\ \tilde{\theta} \end{pmatrix}$$

where $\tilde{\rho}$ and $\tilde{\theta}$ respectively stand for translational and rotational amount of motion.

5. Simulation and Noise Injection

The simulated images are generated using the sensor model$^{2)}$ given in Table 1 and a Gaussian noise model for both positional and magnitude noise. As the sensor has a FOV of $42^o \times 42^o$ and resolution of $937px \times 937px$, a pixel in the image is assumed to cover a FOV calculated as follows.

$$FOV\ of\ one\ px = \left(\frac{42^o}{937px}\right)^2 = 0.04482^o \times 0.04482^o$$

The characteristics given in Table 1 are assumed in generation of the simulated image given in Fig. 2, except that the magnitude limit is lowered to 3.8 mag for the sake of a better illustration. Subsequently, the process of noise injection is implemented on the generated image. Respectively, positional noise and magnitude noise are added to the simulated image.

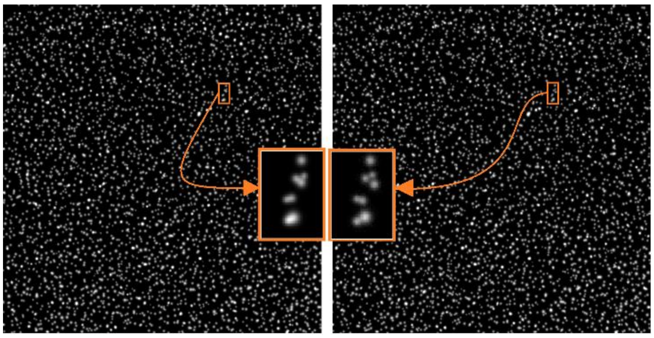

Fig. 2. A couple of star images obtained from the Hipparcos database without noise at the left-hand side and with noise injected at the right-hand side.

Fig. 2 shows two images generated with a magnitude limit 3.8 mag, a FOV $42^o \times 42^o$ and a resolution $937px \times 937px$. Both images are bounded by an interval of right ascension $\alpha \in [0^o, 42^o]$ and of declination $\delta \in [0^o, 42^o]$. Two types of noise are injected, positional noise and magnitude noise. For a better revelation of the effects of noise a smaller patch is extracted and zoomed in. the patch has a FOV $2^o \times 2.7^o$ corresponding to a resolution $45px \times 62px$, and it is located within $\alpha \in [28.1^o, 30.1^o]$ and $\delta \in [29.2^o, 31.9^o]$.

The stars are generated using a 2D Gaussian function, center of which is located on the position of the star given in the catalog, that is, the mean and variance of the function are the exact location and the magnitude of the corresponding star respectively. The addition of positional noise is carried out by imposing a shift effect on the centroid of a star through an individual Gaussian function along horizontal and vertical axes of the image frame. In this example, the amount of positional noise is determined by a normal distribution

$$N(\mu_p, \sigma_p)$$

with a mean $\mu_p = 0$ and variance $\sigma_p = 1$ in terms of pixel. The amount of magnitude noise is also determined by a normal distribution

$$N(\mu_A, \sigma_A)$$

with a mean $\mu_A = 0$ and variance $\sigma_A = 5$ in terms of pixel intensity. The effect of both types of noise is clearly observable in the enlarged patch, where the positions of stars are shifted and the pure Gaussian shape of stars in the left-hand side are slightly degraded in the image at the right-hand side.

6. Case Study

The simulation tools are used in the implementation of the complete process of false star removal and motion estimation. Fig. 3 shows two images that are assumed to represent the images captured at time t and at time $t + 1$ respectively. The image at t at the left-hand side contains six stars picked from the database catalog in compliance with a magnitude limit of 12.6 mag in the region bounded by $\alpha \in [42^o, 42^o]$ and $\delta \in [42^o, 42^o]$. The image at $t + 1$ at the right-hand side is a regeneration of the first image by shifting it -5^o in the direction of declination and rotating 10^o counterclockwise. Also, there is no non-star object in both images. While the amount of shifting and rotation is identical for each star, the non-star object is replaced arbitrarily in the images. The threshold values used in the example are $\epsilon_A = 10$, $\epsilon_d = 3px$ and $\epsilon_m = 1^o$. The process outputs the object labeled with number 3 as a non-star object in the first image and the one labeled with number 1 as a non-star object in the second image. Also, the method can match the stars, thereby it is possible to estimate the amount of shifting and rotation of the sensor.

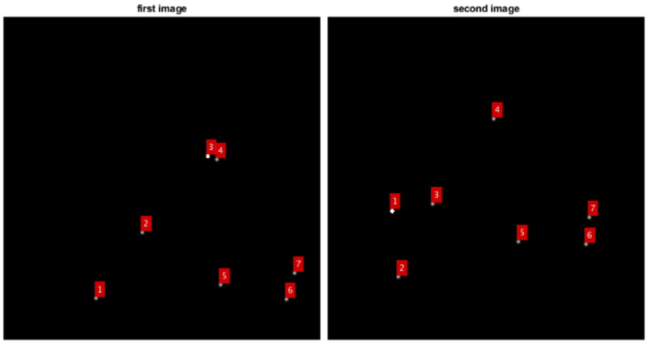

Fig. 3. Two consecutive simulated images that are used in false star removal and camera motion estimation.

In the process, firstly, the objects are detected through a blob analysis, and the area (number of pixels) and centroid of the objects are extracted. The red labeled numbers are assigned to each object in the frames independently. The labels are matched in the end of the process as outputs. Centroid is calculated by means of the method of center of gravity such that

$$\vec{c} = (x, y) = \left(\frac{\sum_i p_i \times x_i}{\sum_i p_i}, \frac{\sum_i p_i \times y_i}{\sum_i p_i}\right)$$

where $\vec{c}$ is the center of gravity, and p_i, x_i and y_i are intensity and position components corresponding to each pixel. The magnitude A is estimated by averaging the pixel intensity over the region of object in terms of number of pixels as follows

$$A = \frac{\sum_{i=1}^{N} p_i}{N}$$

where p_i is pixel intensity, and N is the number of pixels assigned to the object.

After star detection and centroiding, two feature vectors sets are generated for each image frame, containing 21 vectors for 7 objects in both frames. The disparity list is generated using the feature vectors, which contains $21 \times 21 = 441$ disparity vectors. Note that the labels are reserved beside each vector in the disparity list in order not to lose information to be used for matching.

The star matching algorithm intakes the disparity list and the tolerance values to evaluate whether any vector in the disparity list remains lower than the tolerances of magnitude ϵ_A and angular separation ϵ_d. If this is the case, the objects corresponding to these vectors are labeled as candidates of star objects. A subsequent process also checks whether the star candidates satisfy the criterion enforced by the slope tolerance ϵ_m. Accordingly, the star objects are matched such that the labels 1, 2, 4, 5, 6 and 7 in the first image are matched to the labels 2, 3, 4, 5, 6 and 7 in the second image in the given order. The label 3 in the first image and the label 1 in the second image are not matched, thus being assumed to be non-star objects. In the simulation, it is assumed that $\epsilon_A = 10$, $\epsilon_d = 3px$ and $\epsilon_m = 1$. In this regard, in the disparity list, the difference of pixel intensities varies between $(3.5, 9.5)$ falling under ϵ_A, the difference of angular separation varies between $(0.0021, 2.9126)$ falling under ϵ_d and the difference of angular separation varies between $(9.7463^o, 10.5838^o)$ falling under $\|\epsilon_m - \theta\|$. Thus, the rotational component of motion θ is estimated to be $9.7463^o < \tilde{\theta} < 10.5838^o$, which is actually $\theta = 10^o$.

After estimating the rotational motion $\tilde{\theta}$, the star objects in the second image at time $t + 1$ can be rotated by an angle $-\tilde{\theta}$ as follows

$$\vec{o_\iota}' = R(-\tilde{\theta}) \times \vec{o_\iota}^{t+1}$$

where $R(-\tilde{\theta}) = \begin{pmatrix} \cos(-\theta) & -\sin(-\theta) \\ \sin(-\theta) & \cos(-\theta) \end{pmatrix} = \begin{pmatrix} \cos\theta & \sin\theta \\ -\sin\theta & \cos\theta \end{pmatrix}$ is the rotation matrix, $\vec{o_\iota}^{t+1} = \begin{pmatrix} x_i^{t+1} \\ y_i^{t+1} \end{pmatrix}$ is the rotated star object i in the second frame and $\vec{o_i}' = \begin{pmatrix} {x_i}' \\ {y_i}' \end{pmatrix}$ is the rotated star object i. Then, the distance in pixels between the rotated star object in the second image and the matched object in the first image yields the estimated translational motion, such that

$$\widetilde{\rho_x} = {x_i}' - x_i^t$$
$$\widetilde{\rho_y} = {y_i}' - y_i^t$$

where $\widetilde{\rho_x}$ and $\widetilde{\rho_y}$ are the components of the translational motion.

An example is given for the star object labeled 7 in both images matched in the experiment. The star object 7 in the second image is firstly rotated by an angle $-\tilde{\theta} \in (-10.5838^o, 9.7463^o)$, and then the estimated translational components are obtained by subtracting the rotated component.

$$\vec{o_7}' = \begin{pmatrix} \cos\tilde{\theta} & \sin\tilde{\theta} \\ -\sin\tilde{\theta} & \cos\tilde{\theta} \end{pmatrix} \times \begin{pmatrix} 770 \\ 578 \end{pmatrix}_7^{t+1} \Rightarrow \begin{matrix} 857 < x_7' < 863 \\ 651 < y_7' < 661 \end{matrix}$$

$$\widetilde{\rho_x} = x_7' - 858_7^t \Rightarrow \widetilde{\rho_x} \in (-1{,}5)$$
$$\widetilde{\rho_y} = {y_7}' - 740_7^t \Rightarrow \widetilde{\rho_y} \in (-89, -79)$$

The results imply that the second image is horizontally translated by $\widetilde{\rho_x} \in (-1{,}5) \approx (-0.04^o, 0.22^o)$ and vertically by $\widetilde{\rho_y} \in (-89, -79) \approx (-3.99^o, -3.54^o)$ and rotated by $\tilde{\theta} \in (9.7463^o, 10.5838^o)$ with respect to the first image, while the real values are $\rho_x = 0^o$ and $\rho_y = -5^o$.

7. Conclusions and Future Work

The removal of non-star objects from the images increases the likelihood of commissioning true stars into the algorithm to boost accuracy and reduce complexity. Besides, the motional estimation parameters may provide the subsequent steps of star detection, centroiding or star identification with valuable information to further increase accuracy and decrease complexity.

Though the results achieved in the case study are promising, it is problematic in case of entrance of a new star into the scene in the second image since the new star object would not be matched and labeled as a non-star object. However, this problem may be handled by increasing the number of consecutive images and keeping a log of the star objects in the previous image frames.

In addition to a more comprehensive study that will avoid false labeling mentioned above, this study is intended to be used in the preprocessing phases of future studies.

Acknowledgments

The resources and opportunities offered by Space Systems Design and Test Laboratory at Istanbul Technical University are appreciated.

References

1. Aslan, A. R., AlNaimiy, H. M., Fernini, I., Manousakis, A., Shaikh, M., Madara, S. R., Al-Kaabi, T., Karabulut, B., Oztekin, O., Turkoglu, S. and Kalemci, E.: Space Technology Capacity Building in Support of SDG 2030 through CubeSat SharjahSat-1, 9th International Conference on Recent Advances in Space Technologies (RAST), 2019, pp. 955-958.
2. CubeStar Interface Control Document. CubeSpace, 2020. Ver 1.3.
3. Rao, S., Sathyanarayanan, S., Tejaswini, C. and Rohit, B.: Star Sensor Algorithm using the Overlapping Grid Method for Attitude Determination, 2021, pp. 111-121. doi:10.1007/978-981-16-0873-5_10.
4. Zhang, G.: Star Identification Methods, Techniques and Algorithms, 2017. doi:10.1007/978-3-662-53783-1.
5. Rijlaarsdam, D., Yous, H., Byrne, J., Oddenino, D., Furano, G. and Moloney, D.: A Survey of Lost-in-space Star Identification Algorithms since 2009, Sensors 20, 2020.
6. Rijlaarsdam, D., Yous, H., Byrne, J., Oddenino, D., Furano, G. and Moloney, D.: Efficient Star Identification using a Neural Network, Sensors 20, 2020. doi:10.3390/s20133684.
7. Liu, H., Wei, X., Li, J. and Wang, G.: A Star Identification Algorithm Based on Simplest General Graph, Acta Astronautica 183, 2021, pp. 11-22.
8. You, Z., Li, J., Zhang, H., Yang, B. and Le, X.: An Accurate Star Identification Approach Based on Spectral Graph Matching for

Attitude Measurement of Spacecraft, Complex & Intelligent Systems 8, 2022, pp. 1639-1652. doi:10.1007/s40747-021-00619-z.

9. Schulz, V. H., Marcelino, G. M., Seman, L. O., Barros, J. S., Kim, S., Cho, M., Gonzalez, G. V., Leithardt, V. R. Q. and Bezerra, E. A.: Universal Verification Platform and Star Simulator for Fast Star Tracker Design, Sensors, 21, 907, 2021. doi:10.3390/s21030907.

10. Wang, G, Lv, W., Li, J. and Wei, X.: False Star Filtering for Star Sensor Based on Angular Distance Tracking, IEEE Access, Vol 7, 2019, pp. 62401-62411. doi:10.1109/ACCESS.2019.2915976.

11. ESA: The Hipparcos and Tycho Catalogues. ESA SP-1200, 1997.